POLITECNICO DI TORINO
Repository ISTITUZIONALE

Study of flow-induced crystallization in polyvinylidene fluoride 3D printing

Original
Study of flow-induced crystallization in polyvinylidene fluoride 3D printing / Lannunziata, E., Fiorillo, C., Minetola, P., Edeleva, M., Cardon, L., Iuliano, L.. - In: INTERNATIONAL JOURNAL, ADVANCED MANUFACTURING TECHNOLOGY. - ISSN 0268-3768. - ELETTRONICO. - (2025), pp. 1-13. [10.1007/s00170-025-15139-0]

Availability:
This version is available at: 11583/2997510 since: 2025-02-14T09:03:19Z

Publisher:
Springer-Verlag London Limited

Published
DOI:10.1007/s00170-025-15139-0

Terms of use:

This article is made available under terms and conditions as specified in the corresponding bibliographic description in the repository

Publisher copyright

(Article begins on next page)

19 November 2026

The International Journal of Advanced Manufacturing Technology
https://doi.org/10.1007/s00170-025-15139-0

ORIGINAL ARTICLE

Study of flow-induced crystallization in polyvinylidene fluoride 3D printing

Erika Lannunziata[1,3] · Chiara Fiorillo[2] · Paolo Minetola[1,3] · Mariya Edeleva[2] · Ludwig Cardon[2] · Luca Iuliano[1,3]

Received: 29 November 2024 / Accepted: 1 February 2025
© The Author(s) 2025

Abstract

This study explores how additive manufacturing processes, specifically fused filament fabrication (FFF) parameters, affect the β-crystallization of polyvinylidene fluoride (PVDF). A key focus is to ascertain if flow-induced crystallization during FFF improves the overall crystallinity, as the polymer melt is subjected to high shear forces during printing, which reduces kinetic barriers to crystallization and influences the resulting morphology. Using a design-of-experiments approach, the effects of extrusion temperature and printing speed were systematically evaluated to assess their impact on crystallinity, characterized through differential scanning calorimetry, Fourier-transform infrared spectroscopy, and polarized optical microscopy. Statistical analysis identified extrusion temperature as the most significant parameter for promoting β-phase formation, with the highest crystallinity observed at an extrusion temperature of 235 °C. In contrast, printing speed appeared to have a limited influence on crystalline phase distribution, indicating that higher production rates may be achievable without adversely affecting material properties. Nevertheless, rheological investigations underscored the role of both extrusion temperature and printing speed in facilitating shear-induced crystallization. These findings provide valuable insights into the optimization of FFF parameters for PVDF-based functional devices, advancing the development of improved piezoelectric and energy harvesting applications while reducing the cost and complexity associated with conventional manufacturing techniques.

Keywords PVDF · FFF · FIC · β-Phase

Abbreviations

ANOVA	Analysis of variance
DSC	Differential scanning calorimetry
DoE	Design of experiments
FFF	Fused filament fabrication
FIC	Flow-induction crystallization
FTIR	Fourier-transform infrared spectroscopy
POM	Polarized optical microscope
PVDF	Polyvinylidene fluoride
S_p	Extrusion speed
T_{ex}	Extrusion temperature

✉ Erika Lannunziata
erika.lannunziata@polito.it

[1] Department of Management and Production Engineering (DIGEP), Politecnico Di Torino, Corso Duca Degli Abruzzi 24, 10129 Turin, Italy

[2] Centre for Polymer and Material Technologies (CPMT), Department of Materials, Textile and Chemical Engineering, Ghent University, Technologiepark, 130, 9052 Ghent, Belgium

[3] Integrated Additive Manufacturing Centre (IAM@PoliTO), Politecnico Di Torino, Corso Duca Degli Abruzzi 24, 10129 Turin, Italy

1 Introduction

Fused filament fabrication (FFF) of polymers is a popular additive manufacturing plastic processing technique known for its versatility, sustainability, affordability, and user-friendly system. It involves the layer-by-layer deposition of thermoplastic filaments to build three-dimensional objects [1]. For high-performance semi-crystalline polymers, FFF presents both opportunities and challenges due to the unique properties of these materials [2]. One opportunity consists of the ability to orient and align the polymer chains. During FFF, both the shear flow within the nozzle and the velocity gradients induced by the deposition process can significantly deform the polymer microstructure. Flow distorts the configuration of polymer chains, and it is believed that this distortion breaks down the kinetic barriers to crystallization and directs the resulting morphology [3]. This phenomenon known as

Published online: 13 February 2025

flow-induction crystallization (FIC) [4] enhances oriented crystallization. As a result, it is a potentially valuable tool for altering the crystalline morphology of the polymer materials resulting in advanced material properties of the 3D-printed objects [5].

Among the high-performance semi-crystalline polymers, polyvinylidene fluoride (PVDF) has gained attention as a promising material due to its unique combination of properties, including chemical resistance, mechanical strength, and the ability to generate piezoelectricity [6]. From the molecular point of view, PVDF is a thermoplastic semi-crystalline polymer with well-known polymorphism resulting in multiple crystalline phases that significantly influence its properties and applications [7]. In particular, PVDF crystallizes into several polymorphs, α, β, γ, δ, and ε, where α, β, and γ phases are the most commonly seen over the molten crystallization. The α-phase is the most stable and prevalent form, and the α-phase with its *trans-gauche* (TGTG′) conformation crystallizes more readily under quiescent conditions [7] due to its lower energy barrier compared to the all-*trans* (TTTT) conformation of the β-phase [8]. The β-phase, known for its superior piezoelectric, pyroelectric, and ferroelectric properties, is typically achieved through advanced technologies that induce permanent polarization and molecular chain alignment, such as mechanical stretching, high-pressure application, melt quenching, poling under strong electric fields, and electrospinning [9].

Although there have been significant improvements in these areas, there are still limitations, such as the cost and the feasibility of utilizing these techniques to create energy-harvesting or sensing devices with more intricate geometries or scales. These constraints have motivated researchers to explore alternative approaches, such as the development of electroactive PVDF filaments for 3D printing via material extrusion.

In this context, Saleh et al. [10] focused on the optimization of the electroactive PVDF filament production, both with and without additives, using a micro compounder followed by post-treatment (mechanical stretching or electric poling). They attained the highest β-phase fraction (ca. 80%) by fabricating pure (i.e., without additives) PVDF filament through extrusion at 220 °C and mechanical stretching with an average of 4.5 times. While mechanical stretching proved more effective than electric poling in enhancing β-phase content, the latter significantly increased the output current compared to commercially available PVDF filaments. Similarly, Porter et al. [11] investigated the fabrication of PVDF thick films using FFF under various parameters, including in situ electrical poling. Although they could not perform statistical analysis, their results suggested that lower extrusion temperatures, faster extrusion rates, and higher hot-end voltages were favorable for β-phase formation. However, they found that as-printed films exhibited minimal piezoelectricity, and post-printing poling was required to induce measurable piezoelectricity [11].

In addition, some researchers incorporated fillers to induce the generation of β-phase in the FFF 3D-printed PVDF films such as tetraphenylphosphonium chloride, ionic liquid [12], and trifluoroethylene [13]. These additives have led to a significant increase in β-phase content, but they also cause an increase in production times and costs a necessity for additional safety measures. Despite the growing interest toward the use of innovative printing processes, the literature lacks systematic studies on how the 3D-printing process affects the final PVDF crystalline structure.

It is well established that extrusion processes subject the amorphous molten polymer to high shear forces, causing polymer chains to orient and stretch. This orientation reduces the system's entropy, which, in turn, elevates the equilibrium melting temperature, providing additional undercooling that triggers crystallization [8]. Consequently, flow can induce the transition of α to the β-phase by promoting the all-*trans* conformation, thereby accelerating crystallization kinetics and eventually enhancing electroactive properties. Thus, flow-induced crystallization represents a promising approach for increasing crystallinity and engineering specific crystalline phases. However, the relationship between shear forces, crystallinity, and the electroactive properties of PVDF during 3D printing has not been fully explored.

Consequently, the aim of this work was to address the following research questions:

- Can FIC be harnessed to achieve polarized PVDF samples?
- How does the effect of flow during 3D printing alter crystallinity?

To investigate the FIC, the temperature (T_{ex}) and extrusion speed (S_p) were tuned to examine the influence of different shear rates on the β-phase content in PVDF. A statistical approach was employed to ensure the significance of these parameters on crystallinity, involving a design of experiments (DoE), to select the appropriate parameter range for printing. Analytical techniques, including differential scanning calorimetry (DSC), Fourier-transform infrared spectroscopy (FTIR), polarized optical microscope (POM), and rheology, were utilized to assess crystallinity. The resulting crystalline structures were further analyzed using analysis of variance (ANOVA) to correlate the β-phase content with FFF processing parameters. In conclusion, the potential and limitations of the flow-induced crystallization phenomenon in the production of piezoelectric devices through FFF are discussed.

2 Materials and methods

2.1 Material

The PVDF filament (diameter of 1.75 ± 0.05 mm) was purchased from 3DXTech (3DXTech, Michigan, USA), with the commercial name of FluorX.

2.2 DoE for the variation of the printing parameters

This study employs a DoE framework to investigate the effects of two factors, namely, printing speed (S_p) and extrusion temperature (T_{ex}), on the crystalline structure. The experimental design includes six levels for each factor and three replications for each combination to ensure the robustness and reliability of the results. Therefore, the number of total samples printed in this work was calculated as follows:

$$(\text{N° of levels})^{\text{N° of factors}} \times \text{n° of replica} = 6^2 \times 3 = 108 \text{ samples}$$

Table 1 shows the levels for the printing speed (S_p) and extrusion temperature (T_{ex}) used for the study, for a total of 36 combinations.

For each of the 36 combinations of the conditions, we printed a cylindrical sample with a diameter of 20 mm and a height of 3 mm. The printing geometry was input into the PrusaSlicer software. The samples were printed on the Original Prusa i3 MK3S printer. The other parameters, including the building platform temperature and layer height, were maintained at consistent values of 100 °C and 0.15 mm, respectively. Concerning the range of the parameters selected, the boundaries of the temperature range were identified through a series of printing tests, which demonstrated that fabricating samples without printing issues was not feasible at temperatures below 215 °C or above 265 °C.

2.3 Characterization

Differential scanning calorimetry DSC analyses were carried out using a DSC 214 Polyma Equipment (Netzsch Group, Selb, Germany). Two heating and cooling scans were performed under a nitrogen atmosphere (40 mL/min) from 20 to 400 °C with a heating/cooling rate of 0.5, 5, and 10 °C/min. DSC data allowed us to measure the melting temperatures and enthalpies of the material after process conditions, providing information about the changes in the crystalline fraction. The crystalline fraction was evaluated as

$$X_c(\%) = \frac{\Delta H_m}{\Delta H_m^0} \times 100 \quad (1)$$

where ΔH_m is the experimental enthalpy of melting, calculated by the integration of the melting endothermic peak, and ΔH_m^0 is the theoretical melting enthalpy of a purely crystalline PVDF, which was assumed to be equal to 104.7 J/g [10].

Fourier-transform infrared spectroscopy FTIR analysis was carried out with the Bruker Tensor 27 in combination with the OPUS software. The applied spectral range was 600–1500 cm^{-1}, with a resolution of 2 cm^{-1}, and 64 scans in attenuated total reflection mode were collected per sample [10]. The fractions of the different phases were calculated following the approach previously employed by Ye et al. [14]. The initial phase involved assessing the α and β, γ-fractions (F_α and $F_{\beta,\gamma}$) as.

$$F_\alpha = \frac{A_{763}}{A_{763} + A_{840,832}} \times 100 \quad (2)$$

$$F_{\beta,\gamma} = 100\% - F_\alpha \quad (3)$$

where A_{763} and $A_{840,832}$ are the absorbance intensities at 763 cm^{-1} for α-phase and 840/832 cm^{-1} for β- and γ-phases, respectively. Following this, the individual fractions of β- and γ-phases (F_β and F_γ) were calculated by.

$$F_\beta = F_{\beta,\gamma} \times \frac{A_{1276}}{A_{1276} + A_{1233}} \times 100 \quad (4)$$

$$F_\gamma = F_{\beta,\gamma} \times \frac{A_{1233}}{A_{1276} + A_{1233}} \times 100 \quad (5)$$

where A_{1276} and A_{1233} are the absorbance intensities at 1276 and 1233 cm^{-1} that are exclusive for the β- and γ-phases, respectively. The FTIR spectra were processed using the EssentialFTIR software. Initially, they were normalized according to the 1070 peak [11], and the intensities of the characteristic peaks (763, 840, 1233, 1276 cm^{-1}) were exported.

Polarized optical microscope POM was used to observe the morphology of crystalline phases in samples on a Keyence VHX-7000 instrument. The samples were prepared using a microtome (Leica RM2245).

Table 1 Process parameters including printing speed (S_p) and extrusion temperature (T_{ex})

T_{ex} (°C)	S_p (mm/s)
215	15
225	25
235	35
245	45
255	55
265	65

Rheological properties The effect of the different printing temperatures and extrusion speeds was investigated by analyzing the rheological properties of the samples with an Anton Paar rheometer (MCR 702) equipped with a CTD600 oven. We used plate-plate geometry with a 25-mm diameter. Rheological data were collected from 3D-printed discs (25 mm diameter and 1 mm thickness). Rotational rheological measurements were performed to characterize the polymer's steady-state viscosity as a function of shear rate. The shear rate range analyzed was between 0.01 and 10 s^{-1}.

The shear-induced crystallization measurements were conducted according to the heating scheme in Fig. 1. The samples were loaded at a temperature of 180 °C in the rheometer and kept at this temperature for 5 min to erase the thermal history. Then, before the start of the measurement, the samples were cooled down to 160 °C. The temperature was selected close to the crystallization temperature verified with additional DSC measurement. When the measure started, the samples were subjected to a shear flow with constant shear rates. The range values of the shear rate investigated were 0.01, 0.1, and 1 s^{-1}.

3 Results

3.1 Experimental determination of the crystalline phase in the printed samples

The fraction of crystallinity can be determined via DSC and FTIR analyses. Figure 2 presents the first heating cycle of the DSC for the polymers printed at the lowest and highest S_p, within the selected temperature range, to show the processing-induced crystallinity. The DSC analysis can detect the presence of different phases by resolving the melting peaks of each crystalline phase. The melting temperature for

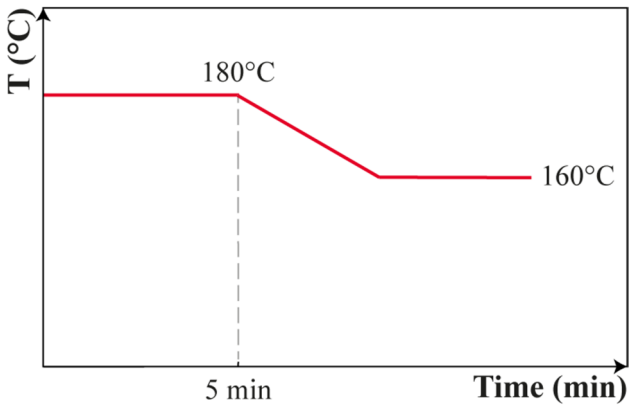


Fig. 1 Heating cycle used for the rheological test to study the shear-induced crystallization

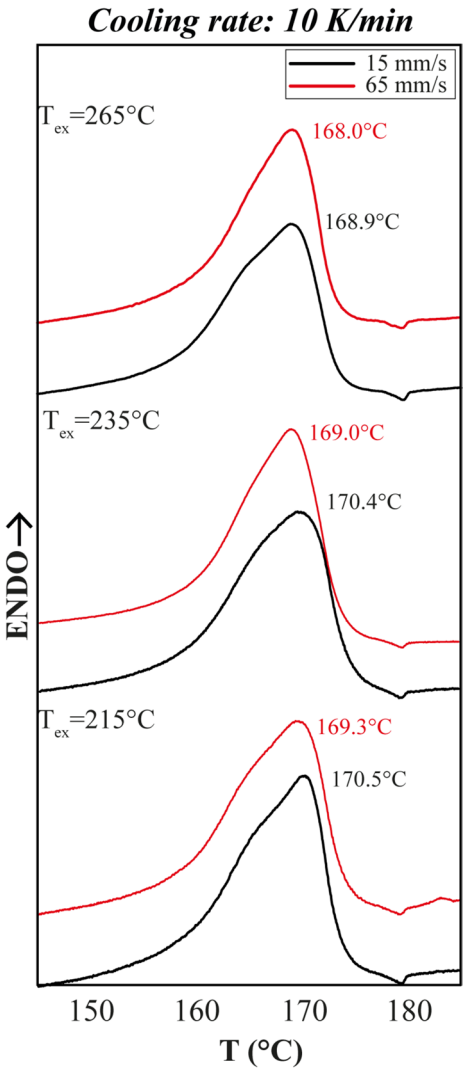


Fig. 2 DSC results for the samples printed at the highest, medium, and lowest T_{ex} with a cooling rate of 10 K/min. The black curves correspond to the lowest printing speed and the red curves to the highest speed

α-, β-, and γ-phases are 167, 172, and 180 °C, respectively [15]. However, at a heating rate of 10 °C/min, the γ-peak was not detected from the DSC analysis. As shown in Fig. 2, we did not observe a well-defined unique melting peak which can be linked to the suboptimal heating/cooling rate. Fan et al. [15] used different cooling rates to reveal the nature of the multi-peak phenomenon of multiple crystalline phases. Therefore, Fig. 3a and b show the DSC trace obtained at 5 and 0.5 °C/min, respectively. Indeed, the lower cooling rates resulted in two different melting peaks, one closer to the α melting point and one closer to the β melting point. Decreasing the cooling rate reveals that the melting peak at a higher temperature exhibits a larger area for the sample printed at 235 °C at 15 mm/s. This result suggests a greater contribution of the β-phase compared to the α-phase in the

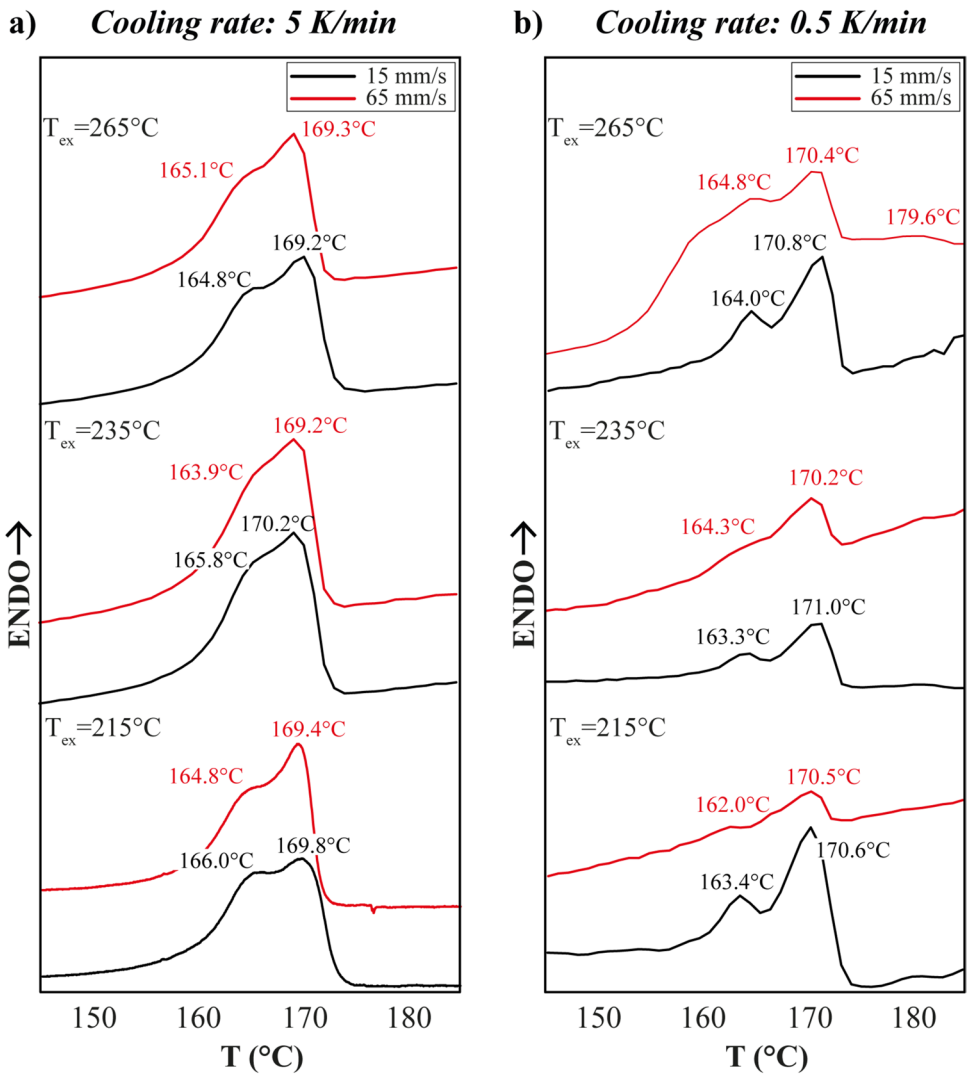


Fig. 3 DSC results for the samples printed at the highest, medium, and lowest T_{ex} with a cooling rate of 5 K/min (**a**) and 0.5 K/min (**b**). The black curves correspond to the lowest printing speed and the red curves to the highest speed

sample's crystallinity. The study of the DSC traces at different cooling rates was also conducted on the filament before printing, and the results are shown in Fig. 4. In this case, lower cooling rates resulted in two distinct melting peaks, with the peak corresponding to the β-phase exhibiting a significantly larger area than that of the α-phase. Additionally, no peak was observed around 180 °C in this analysis either.

As the melting peaks of α- and β-phases overlap on DSC and no deconvolution can be easily performed, we used FTIR to clarify the presence of polymorphism, as FTIR is a complementary method to quantify different crystalline phase contents in a sample.

Figure 5 summarizes the results from the FTIR analysis by comparing the spectra of samples printed at different temperatures at the lowest and highest speeds and the filament, respectively, in Fig. 4a and b. Comparing the spectra of the printed samples, it is immediately obvious that for the α-phase, the peak at 763 cm^{-1} remained mostly constant, except at a temperature of 235 °C, where at both high printing speeds and especially at low printing speed, it tended to decrease significantly in favor of an increase in the β-phase, both at the peaks of 840 and 1276 cm^{-1}. Regarding the γ-phase, the relative peaks were limited, providing the reason why we did not observe the melting peak at 180 °C. In general, simply observing the spectra does not make it easy to distinguish the contribution of γ from that of β, particularly concerning the peaks at 840 and 832 cm^{-1}.

Therefore, Eqs. (2) to (5) were used to evaluate the phase content and separate the two contributions. The results of these calculations are shown in Fig. 6 in the form of a color map, where for each phase the color intensity depends on the phase crystallization fraction percentage; the details are described in [16]. These results also highlight that the α-phase (F_α) is predominant, with the only exception at 235 °C. There does not appear to be a characteristic growth trend of one phase over the others.

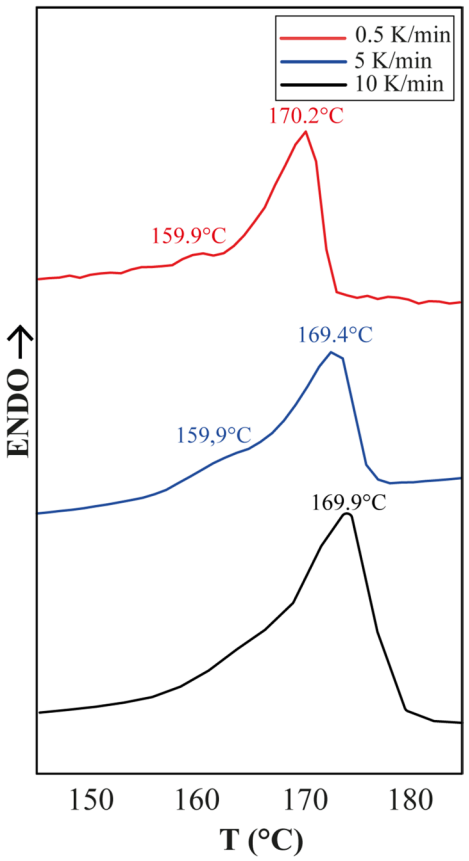


Fig. 4 DSC results for the commercial filament recorded at a cooling rate of 10 K/min (black line), 5 K/min (blue line), and 0.5 K/min (red line)

Now, the FTIR results of the printed samples and the filament are compared. Figure 5 indicates that in the filament spectra, the peaks related to the α-phase were almost absent, while those related to the β- and γ-phases were clearly visible. The β- and γ-phase contributions for the filament were also calculated using Eqs. (2) to (5), revealing that the cumulative percentage of the $F_{\beta,\gamma}$ was approximately 82% (F_β=40%, F_γ=43%). This result is consistent with the findings reported in a previous article [10]. The only sample that recorded a similar value is the one printed at 235 °C at 15 mm/s, with a β-fraction value of 53% (F_β=38%, F_γ=15%).

3.2 Effect of process parameters on crystallinity percentage and melting temperature

Figure 7 shows the results of the ANOVA about the effect of the extrusion temperature and printing speed on the DSC analysis; the response variables are the melting enthalpy ΔH_m, which is used for the total crystallinity estimation in Eq. (1), and the melting temperature T_m (recorded at the cooling rate of 10 K/min). For both response variables, the significance level is set at 95%. The ANOVA tables and the residual plots are collected in the supplementary material (S1). Figure 7a shows the ANOVA results on the total crystallinity. It reports a p-value lower than 0.5% for both the factors T_{ex} and S_p. Therefore, it is possible to assume with a probability of 95% that both extrusion temperature and speed have significant effects on the response variable. The interaction between temperature and speed ($T_{ex} \times S_p$) is not statistically significant, with an F-value of 1.34 and a p-value of 0.168, suggesting no significant combined effect. Therefore, the interaction contribution was excluded from the analysis as an ineffective parameter [17]. Moreover, higher temperature generally leads to higher crystallinity, although the dependence is not entirely linear as seen at 235 and 245 °C. The effect of the printing speed requires further clarification, but the correlation between speed and crystallinity appears to be strongly nonlinear. In addition, the ANOVA was also conducted to investigate the effect of printing parameters on the melting temperature, including extrusion temperature, speed, and their interaction; the results are reported in Fig. 7b. The sole factor that affects the melting temperature is the extrusion temperature. The main plot exhibits the relationship between extrusion temperature and melting temperature. When comparing this plot to the one in Fig. 7a, it can be noticed that the influence of T_{ex} on ΔH_m and T_m are opposite; greater extrusion temperatures favor a higher percentage of crystallinity but lower melting temperature. Figure 7a and b also present the enthalpy and melting temperature values obtained from a DSC analysis of the filament, indicated by a black dashed line, to highlight the effects of the printing process parameters on the material. It can be observed that at low extrusion temperatures, there is a slight increase in both the total crystallinity and the melting temperature. However, as the extrusion temperature increases, there is a sudden rise in crystallinity and a drastic reduction in the melting temperature.

3.3 Effect of process parameters in β-phase fraction formation

ANOVA was also conducted for the β-phase fraction formation calculated by Eq. (4). Before performing the analysis, the normality of the β-phase distribution was verified, but the probability plot recorded a p-value < 0.005. Thus, it is impossible to exclude with 95% confidence that the β-phase distribution is normal. Consequently, the β-phase distribution was transformed using the Johnson transformation to achieve normality. Subsequently, ANOVA was performed, and the results are presented in Fig. 8. Similar to the melting temperature in DSC shown in Fig. 7b, the only factor that appears to have an influence is the extrusion temperature. Thus, the results for the same extrusion temperature at different speeds have been considered as

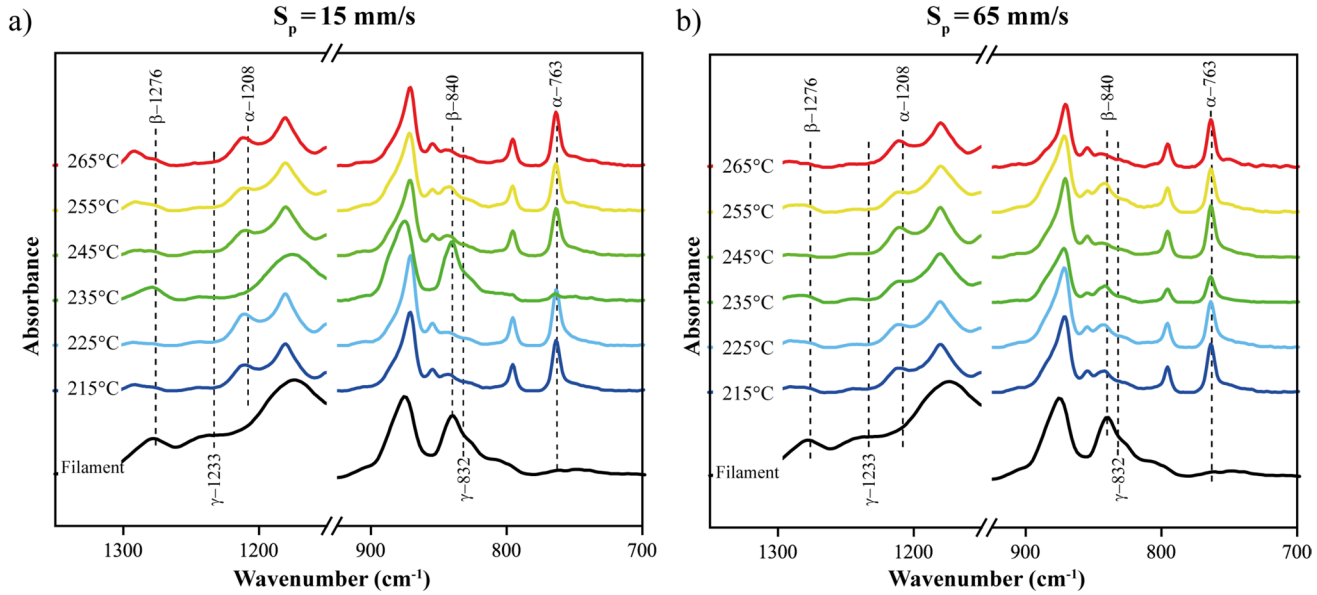


Fig. 5 FTIR spectra comparison of samples printed with different temperatures at 15 mm/s (**a**) and 65 mm/s (**b**). Different curves define different extrusion temperatures: red (265 °C), yellow (255 °C), light green (245 °C), green (235 °C), pale blue (225 °C), dark blue (215 °C), and filament (dark)

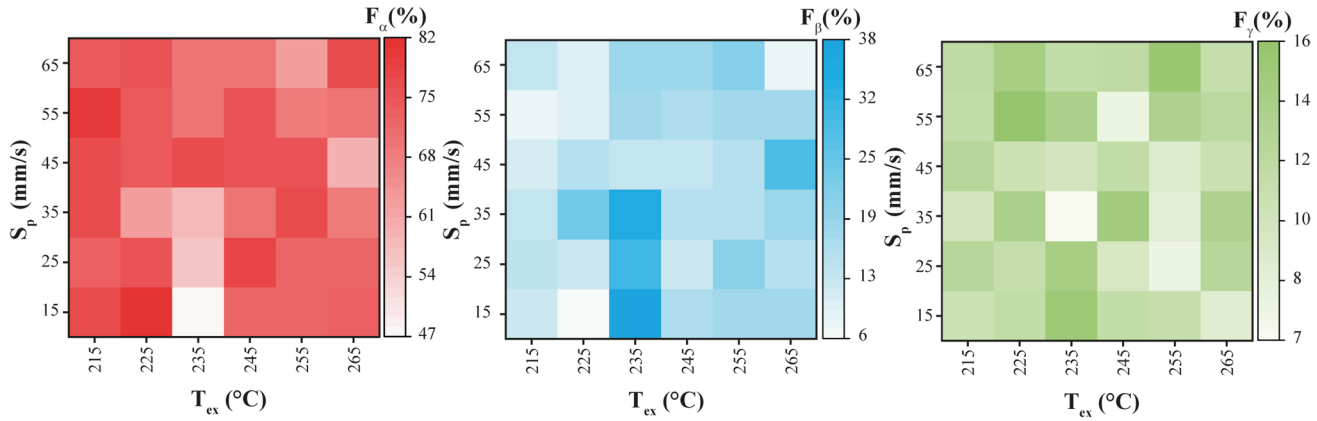


Fig. 6 Maps of phase area at different extrusion temperatures and speed

replicates. The one-way analysis indicates that the *p*-value for T_{ex} is 0.4%, which suggests a 99.6% probability that the extrusion temperature has a significant effect on the β-phase percentage. Contrary to the assertions made by Porter [11], the observation of the main effect plot reveals that the β-phase percentage increases with rising extrusion temperatures. However, as shown also in Figs. 2, 3, and 4, the extrusion temperature at 235 °C reaches the maximum β fraction value. Nevertheless, it is important to emphasize that all the printed samples exhibit a non-negligible percentage of the β-phase directly from the melt. This result highlights the effect of flow on the crystallization of PVDF, as in quiescent crystallization only the pure α-phase forms [4].

3.4 Effect of process parameters on crystalline morphology

This section leads to further investigation of the effect of printing parameters on the PVDF flow-induced crystallization. Since the previous sections point out that the main parameter that influences the crystals is the extrusion temperature, it was decided to analyze samples printed at different temperatures but with the same printing speed of 35 mm/s. The literature frequently states that the melting temperature is mainly related to the thickness of the crystals. Therefore, in this analysis, the radius of the spherulitic crystals was calculated, as shown in the images in Fig. 9. Various optical microscope images were taken at the same

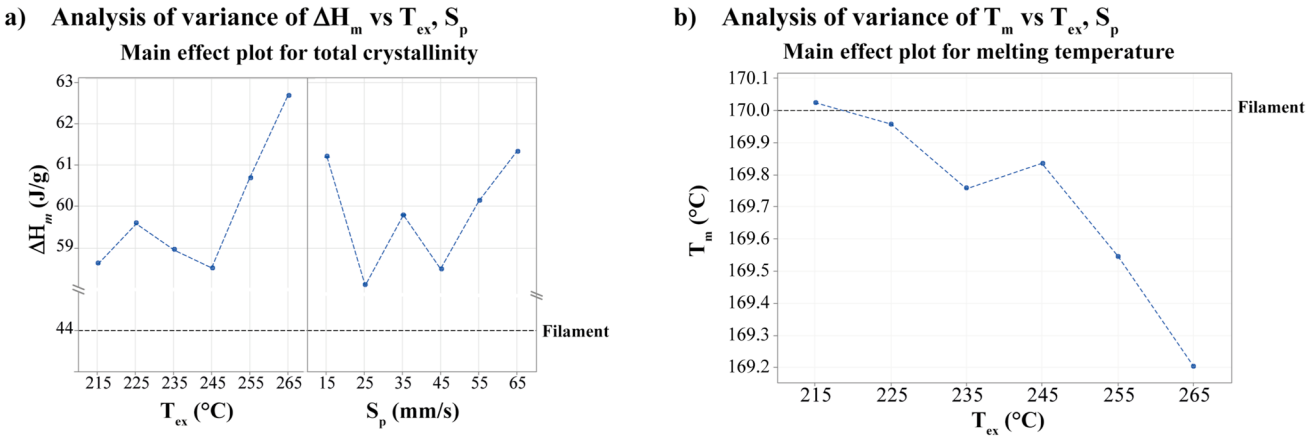


Fig. 7 Analysis of variance where the response variable is the melting enthalpy in (**a**) and the melting temperature in (**b**)

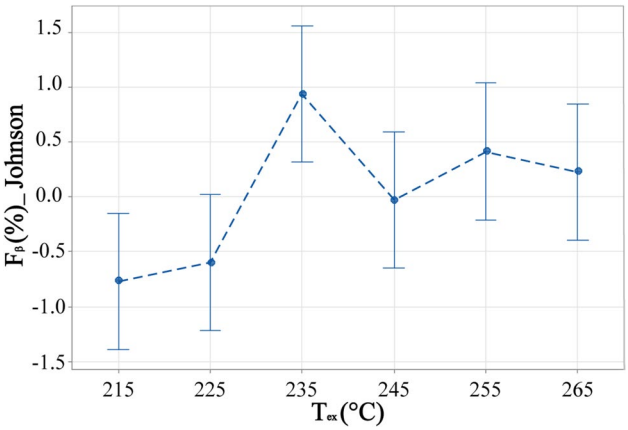


Fig. 8 Analysis of variance where the response variable is the β-fraction (transformed by the Johnson method)

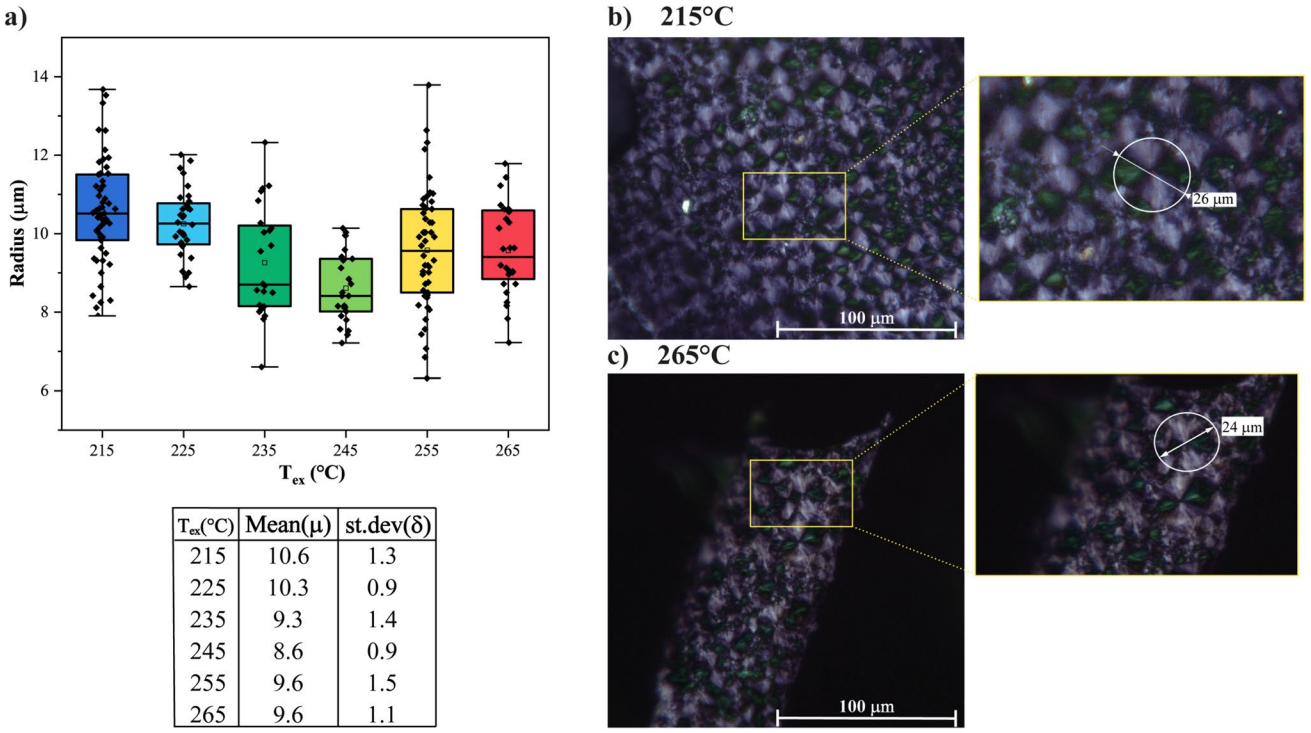
magnification (1000×) for each specimen and the radii of ca. 20 crystals were measured. The mean and distribution of the crystal size obtained from these measurements are reported in the graph in Fig. 9a. Considering the average radii with respect to the extrusion temperature, a trend like that observed for the melting temperatures is noted; specifically, lower extrusion temperatures lead to a higher melting temperature and a larger crystal radius. Previous studies [18] have demonstrated that applying flow at higher temperatures leads to an increase in the density of crystallization nuclei and the formation of spherulites with smaller diameters due to the enhanced crystallization rate at higher temperatures. However, this trend is not strictly decreasing, and it should be noted that the distribution of radii at higher extrusion temperatures is broader compared to those recorded at lower temperatures.

3.5 Effect of process parameters on molecular properties and shear-induced crystallization as measured by rheological test

The results in the previous sections suggest that no influence of S_p exists on the printed samples: the crystallinity is independent of the shear induced by the printing speed. This is, however, counterintuitive, as shear effects on the molecular level degradation and thus crystallization behavior are well described in the literature. To get a deeper insight into the influence of shear due to the printing speed, we performed a rheological investigation of the samples. First, we performed amplitude speed tests to evaluate the molecular degradation. Next, we designed a special experiment of crystallization rate measurement via rheological test. For that, we selected samples printed at different T_{ex} and studied the crystallization rate for them. It is known that the viscosity increases due to the crystallization process. Thus, steady-state viscosity measurements at the crystallization temperature can evaluate the rate of crystallization providing additional insights.

Figure 10 illustrates the viscosity (η) versus shear rate ($\dot{\gamma}$) behavior of 3D-printed samples printed at various temperatures and measured at a constant temperature of 180 °C. Subplot in Fig. 9a shows the three different plot lines which correspond to the PVDF sample printed at the lowest, medium, and highest extrusion temperature. Subplot Fig. 9b shows the difference in the viscosity behavior for the samples printed at different S_p.

For the samples printed at different temperatures (Fig. 10a), we observe a clear difference in the zero-shear viscosity (η_0) at low shear rates which is linked to the average molar mass. The value of zero-shear viscosity decreases as the T_{ex} increases confirming the thermal degradation of the polymer via chain scission mechanism leading to the reduction in the Mn value and thus η_0.



T_{ex}(°C)	Mean(µ)	st.dev(δ)
215	10.6	1.3
225	10.3	0.9
235	9.3	1.4
245	8.6	0.9
255	9.6	1.5
265	9.6	1.1

Fig. 9 Mean and distribution of the crystal radius at different extrusion temperatures (**a**); POM analysis of the 215 °C (**b**) and 265 °C printed samples (**c**)

Another interesting behavior to point out is the changing of the curve shape between the material processed at 215 °C and the other two. For the samples extruded at 215 °C, the shear thinning happens more abruptly than for the others. The reason could be due to the fronting of the molar mass distribution of the polymer due to the formation of oligomers [19]. This is linked to a type of degradation process happening by chain scission, which increases the number of smaller oligomers.

In Fig. 10, the data were fitted using the Carreau model in this formulation:

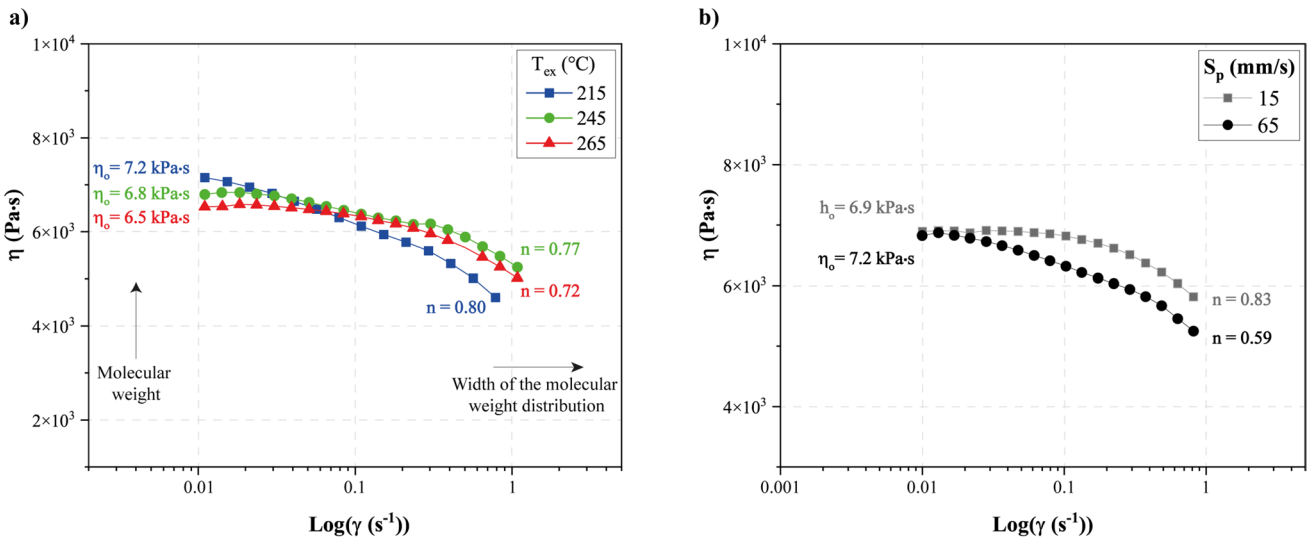


Fig. 10 Effect of process parameters on viscosity at different shear rates at 180 °C for three different extrusion temperatures (215, 245, 265 °C) (**a**) and for the lowest and highest printing speed (15 and 65 mm/s) printed at 245 °C extrusion temperature (**b**)

$$y = \eta_{inf} + \left(\eta_0 - \eta_{inf}\right)\left[1 + (tx)^a\right]^{\frac{n-1}{a}}$$

where η_{inf} is the viscosity for an infinite value of shear rate (corresponding to the value at the second Newtonian plateau), η_0 is the viscosity for a low value of shear rate (corresponding to the value at the first Newtonian plateau), a is the transition control factor, and n is the power index. The slope of the curve corresponds to n^{-1} and it is an indication of the magnitude of the shear thinning effect which is strongly affected by the dispersity of the polymer. In fact, we notice that the n increases for lower T_{ex} indicating that the dispersity increases. This is consistent with the degradation of the polymer via the chain-scission mechanism with the formation of oligomers [20].

According to the literature data, PVDF thermal degradation consists of two different mechanisms. One of them includes the scission of the C–H bond followed by the C–F bond. The other consists of backbone scission with consequent formation of halogenated compounds. Silva et al. [21] showed that in the presence of any solvent, the main mechanism is represented by the first one. However, the presence of alkali promotes the chain-scission process [22].

Figure 10b shows that for the samples extruded at different S_p, the molecular degradation is also detectable: despite the zero-shear rate viscosity being identical for both samples, the shear-thinning behavior is significantly different, highlighting the decrease of the n value which corresponds to the increase of dispersity. Consequently, we can elaborate that, due to degradation, a lot of oligomers are formed due to the so-called unzipping mechanism. That might have a very subtle effect on the overall crystallization, as the chain mobility changes insignificantly resulting in a negligible influence on the crystallinity.

The shear-induced crystallization rheological tests at 160 °C allowed us to get the insights into the difference in the crystallinity of the samples which cannot be observed otherwise. In Fig. 11, the normalized shear stress growth coefficient is plotted over time. Each sample is identified with its extrusion temperature. Additionally, the induction times are plotted in Fig. 12 for each sample and for each shear rate which corresponds to the different S_p. Overall, we see that for a low shear rate the increase of T_{ex} results in the increase of the induction time. As expected, the higher the shear rate, the closer is the value of induction times. Consequently, we can conclude that the FIC is observed for our samples though it cannot be detected by FTIR and DSC measurements.

The maximum shear rate selected for the investigation was dictated by instrument limitation; it is evidently lower than the one imposed by the printing. However, for the present work, the aim was to uncover the effect of the extrusion temperature on the flow-induced crystallization. Even if the global value of the shear rate at the nozzle exit is higher than the maximum investigated experimentally, our shear rate range allowed us to speculate on the local shear rate of the nozzle area.

At the exit of the die, when the local shear rate is higher, the FIC could be considered uniform for all the T_{ex}. Hence, the difference among the T_{ex} becomes negligible by increasing the shear rate via changing S_p. However, at the core of the filament where shear rates are extremely low, as highlighted in yellow in Fig. 13, lower temperature can promote fast crystallization [23]. Consequently, the crystallinity differs inside the filament and on its surface. The FTIR, however, would detect only the "surface" crystallinity, whereas DSC measures the overall/average crystallinity. The direct crystallinity measurements in the middle of the filament experimentally are rather complicated. Thus, we can derive the conclusion only via indirect observations of the FIC effect.

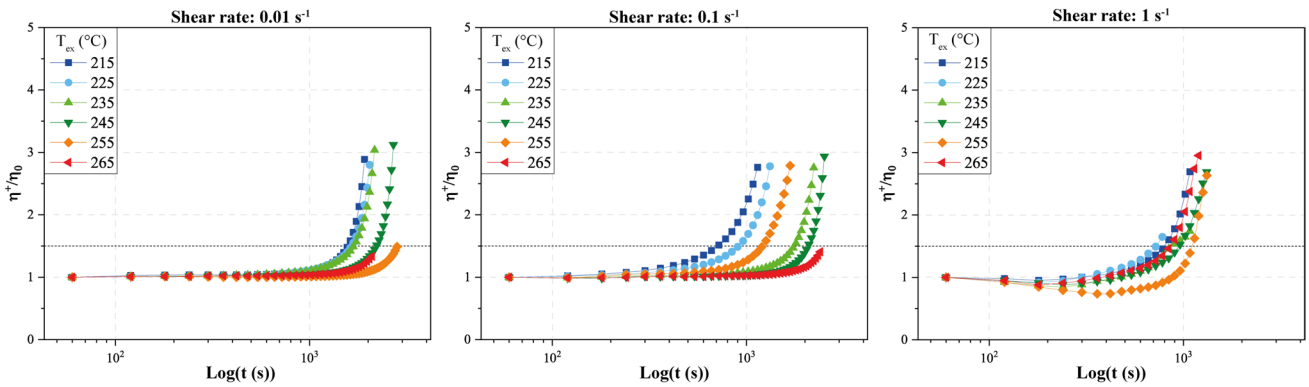


Fig. 11 Effect of different shear stress (0.01, 0.1, and 1 s^{-1}) on the crystallization phenomenon at 160 °C

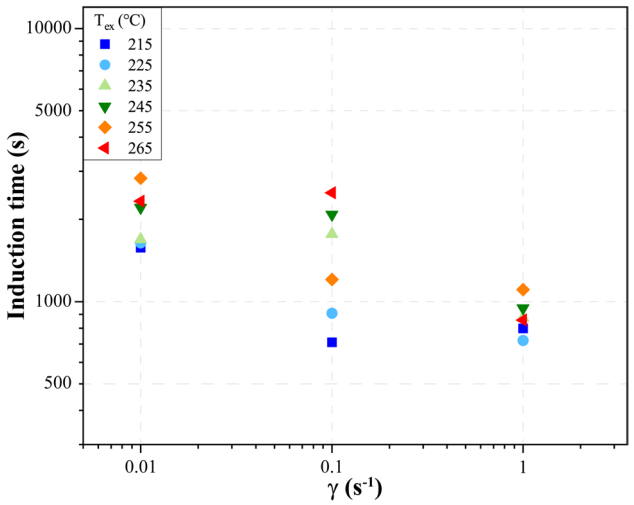


Fig. 12 Induction time over the shear rate range for all the extrusion temperatures involved in this work

4 Discussion

During the FFF process, the molten polymer experiences shear and extensional flows within the nozzle, leading to the orientation and the stretching of polymer chains on the molecular level [24]. This mechanical deformation is critical, as it breaks down the kinetic barriers for crystallization, thereby accelerating the nucleation and growth of specific crystalline phases. This phenomenon is called flow-induced crystallization (FIC). In the context of PVDF, FIC plays a crucial role in promoting the formation of the electroactive β-phase, which is particularly valued for its piezoelectric properties. Indeed, in each printed sample analyzed in this study, a non-negligible percentage of the β-phase is present. This result is a consequence of the effect of flow on crystallization, as under quiescent conditions, the only phase that forms is α-phase [6].

In this study, we elaborate on the impact of extrusion temperature and printing speed on the crystallization behavior of 3D-printed PVDF. The statistical analysis via ANOVA revealed that extrusion temperature is the dominant factor influencing both the overall crystallinity and the β-phase content. The DSC analysis confirmed that higher extrusion temperatures generally lead to an increase in crystallinity, as evidenced by the higher melting enthalpies. However, this increase is not linear, with the most notable enhancement in β-phase crystallization occurring at 235 °C, which suggests an optimal temperature for achieving the desired polymorphic transformation. This is consistent with the findings from the FTIR analysis, where the β-phase fraction was significantly higher at this temperature, particularly at lower printing speeds. This could be attributed to the increased molecular mobility [25] and the favorable thermodynamic conditions that promote the all-*trans* conformation, essential for β-phase formation [18]. On the contrary, at first sight, the printing speed seems to have virtually no effect on crystallization opening the possibility for faster printing and thus faster production of plastic parts. The rheological analysis provided additional insights into the molecular changes occurring at different extrusion temperatures. The decrease in zero-shear viscosity with increasing temperature, although small, suggests potential average molar mass decrease, which could be due to thermal degradation mechanisms via chain scission. Moreover, lower extrusion temperatures seem to decrease the crystallization induction time at a lower shear rate than at the core of the filament. On the other hand, at a higher shear rate, the induction time difference among the different extrusion temperatures becomes negligible.

Interestingly, the study also observed a reduction in melting temperature with increasing extrusion temperature, which could be related to different causes:

1. Degradation. T_m increases as the average molar mass increases and decreases as polydispersity and branching increases [26]. Higher extrusion temperatures lead to more pronounced degradation, resulting in lower average molar mass, as observed in the section on rheology.
2. Crystal stability. Larger and more uniformly distributed crystals were observed at lower extrusion temperatures. Higher extrusion temperatures can lead to a broader distribution of crystal sizes, resulting in less stable crystals. This instability affects the equilibrium melting temperature [27]. This hypothesis is supported by the results of Section 3.4.
3. Relaxation of the polymer chains. The phenomenon of flow-induced orientation is governed by the competition between molecular relaxation and flow strength [4]. Jalali et al. [28] asserted that the chain orientation induced by high shear rates reduces the system's entropy, leading to an increase in melting temperature. Consequently, the increase in extrusion temperature causes chain relaxation, resulting in a reduction in orientation and, therefore, a decrease in melting temperature.

In the interest of thoroughness, it is necessary to highlight that the findings presented in this paper diverge from those commonly reported in the literature with respect to the increase of the β-phase attributed to the FIC phenomenon. Specifically, it is generally expected that the β-phase would increase with rising shear rates, thus favoring extrusion at lower temperatures and higher velocities. However, in our study, the β-phase appears to be primarily governed by temperature, while velocity seems to exert no significant influence. This outcome is attributable to the choice of

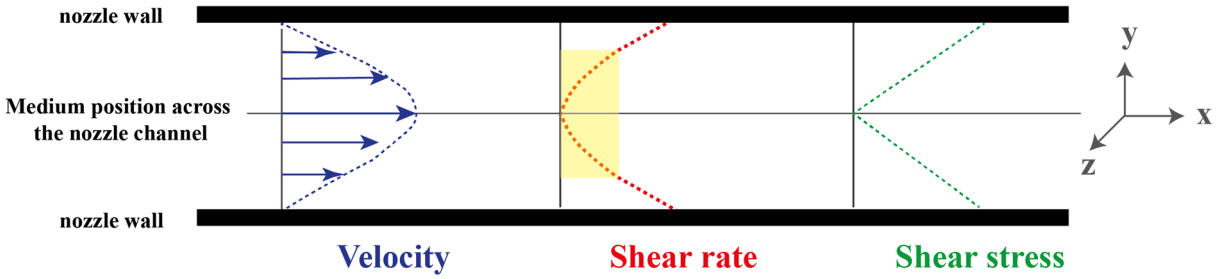


Fig. 13 Velocity, shear rate, and shear stress profile inside the nozzle/filament

maintaining a constant nozzle diameter of 0.4 mm throughout the entire experimental procedure.

Turning our attention to the calculation of the shear rate, described in the supplementary information S2, the range of shear rates examined in this study spans from 23 to 100 s^{-1}. If the nozzle diameter were reduced by half, the shear rate range would extend from 184 to 796 s^{-1}. Such a modification would allow for the investigation of a broader range of applied shear rates, thereby offering a more comprehensive understanding of the influence of shear during the printing process.

5 Conclusion

This study presents a comprehensive investigation of the FFF printing parameters' effect on PVDF crystallization and crystalline morphology. Different analytical techniques demonstrate that extrusion temperature is a critical parameter in controlling the crystallization and polymorphic phase distribution in PVDF during FFF. The findings suggest that an extrusion temperature of around 235 °C is optimal for maximizing β-phase content. The results also highlight the importance of considering rheological behavior and potential thermal degradation when optimizing FFF parameters for PVDF. These findings contribute to the optimization of 3D-printing parameters for producing PVDF-based functional devices with enhanced electroactive properties, such as sensors and energy harvesters. Future research should explore the effect of different shear rates on the piezoelectric PVDF properties during the FFF process by tuning the nozzle diameter. In addition, the process scalability could be included by printing multiple samples within the same process. However, the results indicate that temperature control during printing is the most critical factor in regulating the piezoelectric properties of the material. Consequently, it is essential to print samples individually, positioning each at a different location on the building plate. Moreover, it is fundamental to investigate the PVDF 3D-printed device's long-term stability under various operational conditions and post-printing treatments to maximize the β-phase over the non-polar α-phase.

Author contribution Erika Lannunziata: investigation, methodology, formal analysis, data curation, writing—original draft. Chiara Fiorillo: methodology, data curation. Mariya Edeleva: supervision, conceptualization, data validation, writing—review & editing. Paolo Minetola: supervision, visualization, writing—review & editing. Ludwig Cardon: supervision, review & editing. Luca Iuliano: resources, supervision, project administration.

Funding Open access funding provided by Politecnico di Torino within the CRUI-CARE Agreement. This study was carried out within the Ministerial Decree no. 1062/2021 and received funding from the FSE REACT-EU-PON Ricerca e Innovazione 2014–2020. This manuscript reflects only the authors' views and opinions; neither the European Union nor the European Commission can be considered responsible for them.

Declarations

Conflict of interest The authors declare no competing interests.

Open Access This article is licensed under a Creative Commons Attribution 4.0 International License, which permits use, sharing, adaptation, distribution and reproduction in any medium or format, as long as you give appropriate credit to the original author(s) and the source, provide a link to the Creative Commons licence, and indicate if changes were made. The images or other third party material in this article are included in the article's Creative Commons licence, unless indicated otherwise in a credit line to the material. If material is not included in the article's Creative Commons licence and your intended use is not permitted by statutory regulation or exceeds the permitted use, you will need to obtain permission directly from the copyright holder. To view a copy of this licence, visit http://creativecommons.org/licenses/by/4.0/.

References

1. Hu B, et al (2019) Improved design of fused deposition modeling equipment for 3D printing of high-performance PEEK parts. Mech Mater 137. https://doi.org/10.1016/j.mechmat.2019.103139
2. Lannunziata E, Colucci G, Minetola P, Giubilini A (2024) Effect of annealing treatment and infill percentage on 3D-printed PEEK samples by fused filament fabrication. Int J Adv Manuf Technol 131(9–10):5209–5222. https://doi.org/10.1007/s00170-024-13347-8

3. McIlroy C, Graham RS (2018) Modelling flow-enhanced crystallisation during fused filament fabrication of semi-crystalline polymer melts. Addit Manuf 24:323–340. https://doi.org/10.1016/j.addma.2018.10.018
4. Chu Z, Liu L, Lou Y, Zhao R, Ma Z, Li Y (2020) Flow-induced crystallization of crosslinked poly(vinylidene fluoride) at elevated temperatures: formation and evolution of the electroactive β-phase. Ind Eng Chem Res 59(10):4459–4471. https://doi.org/10.1021/acs.iecr.9b05667
5. Vaes D, Van Puyvelde P (2021) Semi-crystalline feedstock for filament-based 3D printing of polymers. Elsevier Ltd. https://doi.org/10.1016/j.progpolymsci.2021.101411
6. Dallaev R, Pisarenko T, Sobola D, Orudzhev F, Ramazanov S, Trčka T (2022) Brief review of PVDF properties and applications potential. MDPI. https://doi.org/10.3390/polym14224793
7. Sencadas V, Costa CM, Gómez Ribelles JL, Lanceros-Mendez S (2010) Isothermal crystallization kinetics of poly(vinylidene fluoride) in the α-phase in the scope of the Avrami equation. J Mater Sci 45(5):1328–1335. https://doi.org/10.1007/s10853-009-4086-3
8. Chu Z, et al (2020) Effects of strain rate and temperature on polymorphism in flow-induced crystallization of poly(vinylidene fluoride). Polymer (Guildf) 203. https://doi.org/10.1016/j.polymer.2020.122773
9. Lanceros-Méndez S, Mano JF, Costa AM, Schmidt VH (2001) FTIR and DSC studies of mechanically deformed β-PVDF films. J Macromol Sci Phys 40(3–4):517–527. https://doi.org/10.1081/MB-100106174
10. Saleh AA, Melenka GW, Leung SN (2023) Processing-structure–property relationships in the fabrication of extrusion electroactive poly(vinylidenefluoride) filaments. J Appl Polym Sci 140(21). https://doi.org/10.1002/app.53885
11. Porter DA, Hoang TVT, Berfield TA (2017) Effects of in-situ poling and process parameters on fused filament fabrication printed PVDF sheet mechanical and electrical properties. Addit Manuf 13:81–92. https://doi.org/10.1016/j.addma.2016.11.005
12. Tao R, Shi J, Rafiee M, Akbarzadeh A, Therriault D (2022) Fused filament fabrication of PVDF films for piezoelectric sensing and energy harvesting applications. Mater Adv 3(12):4851–4860. https://doi.org/10.1039/d2ma00072e
13. Momenzadeh N, Derakhshani M, Berfield TA (2022) Influences of post-processing treatments on mechanical properties and beta-phase content in material extrusion additively manufactured polyvinylidene fluoride structures. Prog Addit Manuf 7(1):55–64. https://doi.org/10.1007/s40964-021-00212-3
14. Ye Q et al (2024) Chain orientation-dependent polymorphic crystallization of poly(vinylidene fluoride): a guide to achieving polar phases. Macromolecules 57(8):3671–3686. https://doi.org/10.1021/acs.macromol.3c02447
15. Fan Z, Schwedes M, Schwaderer J, Beuermann S, Fischlschweiger M (2022) Molecular weight as a key for electroactive phase formation in poly(vinylidene fluoride). Mater Res Lett 10(4):271–277. https://doi.org/10.1080/21663831.2022.2036840
16. Origin color map. https://www.originlab.com/doc/en/Origin-Help/Heat_map. Accessed: Oct. 09, 2024. [Online]. Available: https://www.originlab.com/doc/en/Origin-Help/Heat_map
17. Moradi M, Aminzadeh A, Rahmatabadi D, Rasouli SA (2021) Statistical and experimental analysis of process parameters of 3D nylon printed parts by fused deposition modeling: response surface modeling and optimization. J Mater Eng Perform 30(7):5441–5454. https://doi.org/10.1007/s11665-021-05848-4
18. Gebrekrstos A, Sharma M, Madras G, Bose S (2016) New physical insights into shear history dependent polymorphism in poly(vinylidene fluoride). Cryst Growth Des 16(5):2937–2944. https://doi.org/10.1021/acs.cgd.6b00282
19. Osswald T, Rudolph N (2015) Structure and properties of deforming polymers. pp 25–58. Accessed: Aug. 21, 2024. [Online]. Available: https://doi.org/10.3139/9781569905234.002
20. Ceretti DVA, Edeleva M, Cardon L, D'hooge DR (2023) Molecular pathways for polymer degradation during conventional processing, additive manufacturing, and mechanical recycling. MDPI. https://doi.org/10.3390/molecules28052344
21. de Jesus Silva AJ, Contreras MM, Nascimento CR, da Costa MF (2020) Kinetics of thermal degradation and lifetime study of poly(vinylidene fluoride) (PVDF) subjected to bioethanol fuel accelerated aging. Heliyon 6(7) https://doi.org/10.1016/j.heliyon.2020.e04573
22. Fairus Rabuni M (2015) The contrastive study of chemical treatment on the properties of hydrophobic PVDF membrane. J Appl Sci Process Eng 2(1). https://doi.org/10.33736/jaspe.163.2015
23. Bakrani Balani S, Chabert F, Nassiet V, Cantarel A (2019) Influence of printing parameters on the stability of deposited beads in fused filament fabrication of poly(lactic) acid. Addit Manuf 25:112–121. https://doi.org/10.1016/j.addma.2018.10.012
24. Aberoumand M, et al (2023) 4D Printing of polyvinyl chloride (PVC): a detailed analysis of microstructure, programming, and shape memory performance. Macromol Mater Eng 308:7. https://doi.org/10.1002/mame.202200677
25. Rahmatabadi D, et al (2023) Development of pure poly vinyl chloride (PVC) with excellent 3D printability and macro- and micro-structural properties. Macromol Mater Eng 308(5). https://doi.org/10.1002/mame.202200568
26. Purushothaman SM et al (2024) Quantifying the crystalline polymorphism in PVDF: comparative criteria using DSC, WAXS, FT-IR, and Raman spectroscopy. ACS Appl Polym Mater. https://doi.org/10.1021/acsapm.4c01157
27. Hoffman JD, Weeks JJ (1962) Melting process and the equilibrium melting temperature of polychlorotrifluoroethylene. J Res Natl Bur Stand. Sect A, Phys Chem 66(1):13
28. Jalali A, Shahbikian S, Huneault MA, Elkoun S (2017) Effect of molecular weight on the shear-induced crystallization of poly(lactic acid). Polymer (Guildf) 112:393–401. https://doi.org/10.1016/j.polymer.2017.02.017

Publisher's Note Springer Nature remains neutral with regard to jurisdictional claims in published maps and institutional affiliations.